

The influence of electric circuit parameters on NO_x generation by transient spark discharge

Mário Janda^{1,*} , Karol Hensel¹ , Zdenko Machala¹  and Thomas A Field^{2,*} 

¹ Division of Environmental Physics, Faculty of Mathematics, Physics and Informatics, Comenius University, Mlynská Dolina, Bratislava 84248, Slovakia

² Centre for Light-Matter Interactions, School of Mathematics and Physics, University Road, Belfast BT7 1NN, United Kingdom

E-mail: mario.janda@fmph.uniba.sk and t.field@qub.ac.uk

Received 15 February 2023, revised 19 June 2023

Accepted for publication 11 July 2023

Published 31 August 2023



CrossMark

Abstract

Nitrogen fixation, production of NO and NO₂ from N₂ and O₂ in air, has been investigated with transient spark self-pulsing DC discharges. NO production is boosted by the addition of capacitors and an inductor to the electrical circuit which drives the discharge. The quantity of NO produced per joule of electrical input energy is doubled, though the quantity of NO₂ produced drops. The yield of NO is also increased because the modified circuit enables higher discharge currents to be used. NO concentrations as high as 2000 ppm were obtained with input energy densities of around 300 J per liter of input gas, whilst NO₂ concentrations were around 150 ppm. This simple modification of the driving circuit may have potential for optimizing the plasma chemistry with other input gas mixtures and for scaling up nitrogen fixation from air.

Keywords: plasma, nitrogen fixation, NO_x production, low temperature plasma, transient spark, driving circuit

(Some figures may appear in colour only in the online journal)

1. Introduction

Sustainable development of our society requires the development of new technologies to establish more environmentally friendly agriculture and industry. Many emerging technologies and processes use non-thermal plasmas (NTP) generated by electrical discharges [1–5]. The key characteristic of NTP is unequal mean energy (temperature) of electrons and heavy particles. While the temperature of electrons can easily exceed 10 000 K, the increase of gas temperature above

room temperature can be negligible [6, 7]. Highly reactive species generated by the energetic electrons in NTP enable chemical reactions to proceed, which would otherwise be too slow at room temperature. For example, NTP in air can be used to generate various reactive oxygen and nitrogen species (RONS), such as ozone, O₃, and the nitrogen oxides, NO and NO₂. The exact chemistry depends on the type of discharge used [8–13]. Nitrogen oxides (NO_x) are unwanted by-products in all combustion processes with air as oxidant, but NTP electrical discharges can produce NO_x at lower energy costs for multiple applications. For example, NO_x molecules are useful because of their antibacterial, cytotoxic, and therapeutic effects [14–16].

Electrical discharges generating NTP have potential to be an alternative future technology for nitrogen fixation [17]. For example, generation of NTP in contact with water enables direct transfer of NO_x and their acids into the liquid phase.

* Authors to whom any correspondence should be addressed.



Original content from this work may be used under the terms of the [Creative Commons Attribution 4.0 licence](https://creativecommons.org/licenses/by/4.0/). Any further distribution of this work must maintain attribution to the author(s) and the title of the work, journal citation and DOI.

Indeed, the generation of NTP in contact with water has become a hot-topic in the last few years [18] because plasmas in contact with water can simultaneously generate several aqueous RONS, such as nitrite NO_2^- , nitrate NO_3^- , peroxy-nitrite ONOO^- , ozone O_3 , and hydrogen peroxide H_2O_2 . The exact composition of the plasma activated water (PAW) varies with the plasma source used and the working gas [19–26]. PAW with different compositions have many potential applications in, for example, seed germination and plant growth promotion [27, 28], pest control [29], wound healing [30] and inactivation of cancer cells [31]. Thus, formation of PAW by direct contact between NTP and water is advantageous and should be studied further.

Transport of active species from plasma (gas phase) into liquid phase is the primary source of RONS in the liquid phase. The rate of gas to liquid transfer depends on the area of the plasma/water interface, which can limit the concentrations of aqueous RONS and their overall chemical effect [18, 32]. The transformation of bulk water into fine droplets in an electrohydrodynamic spray (ES) results in an increase of the plasma/water interface area and can accelerate the transport of gaseous species into water [33, 34]. The idea of using ES microdroplets to increase the plasma-water interface area has been adopted by several research groups [35–37], as well as in our previous work [26, 38]. For example, fine aerosol droplet of water generated by ES have been passed directly through the active discharge zone of transient spark discharges, which produce high NO_x concentrations in air, to prepare PAW. Direct contact of water microdroplets with the discharge resulted in a very efficient transfer of gaseous RONS into water [26].

Transient spark discharges are DC-driven self-pulsing discharges, which produce spark current pulses with typical repetition frequencies of 1–10 kHz [39, 40]. The transient spark current pulses are sufficiently short (~ 10 – 100 ns) to avoid plasma thermalization [40, 41]. Non-equilibrium plasmas generated by transient spark discharges are highly reactive because of their high electron density, typically $\sim 10^{17} \text{ cm}^{-3}$ [41]. The self-pulsing regime is maintained by a large ballast resistor (5–10 $\text{M}\Omega$) placed between the high voltage (HV) DC power supply and the anode. This ballast resistor limits the current drawn from the power supply after the spark, which prevents formation of pulseless DC high pressure glow discharges (GD). There are ohmic energy losses, of course, in the ballast resistor and so it is desirable to minimize the resistance of the ballast resistor to minimize the energy losses. Lower resistances of the ballast resistor, however, allow higher currents and enable formation of GD. Therefore, it is desirable to find a different method to prevent GD formation. In a separate paper we presented a simple modification to the electrical driving circuit for transient spark discharge generation, which uses an additional inductance [42]. The effect of this inductance on the electric characteristics of the transient spark discharge in air and helium is presented and discussed in detail. In this work, the effect of driving circuit modification on the chemical reactivity of transient spark discharges has been evaluated by measuring the concentrations of NO and NO_2 generated with

and without the additional inductance. The energy efficiency of NO and NO_2 production has also been investigated.

2. Experimental setup

A schematic diagram of the experimental apparatus is shown in figure 1. The discharge was generated by a DC HV power supply (Spellman SL30P300) connected to the anode via a series resistor $R = 2$ – $10 \text{ M}\Omega$. The anode was a steel M2 screw with a sharpened tip, while the grounded cathode was a copper wire with a diameter 1 mm (pin-to-wire configuration). The distance between the electrodes was 8–10 mm. Despite using a DC power supply, the electrical circuit shown in figure 1 generates a self-pulsing ‘transient spark’ discharge characterized by short high current pulses (~ 10 A, 10–100 ns), with a typical repetition frequencies, f , of 1–10 kHz [39, 40]. In transient spark, the discharging capacitance is provided by internal capacitance of the circuit ($C_{\text{int}} \sim 25$ pF), given mostly by the cable connecting the anode with the ballast resistor R , and by a HV probe.

In this work we study the effect of additional circuit components, the external capacitor C_{ext} (30–500 pF) and the coil (inductor) L_{ext} (0.73 mH) on the transient spark discharge properties and especially NO_x generation efficiency. These components, C_{ext} and L_{ext} , are optional and are shown in red in figure 1.

The electrical discharge characteristics were measured with a HV probe (North Star PVM-12) and a current probe (Pearson Electronics 2877) connected to a digital oscilloscope (Tektronix TBS2104). When the external capacitance, C_{ext} , was greater than 110 pF, an additional attenuator (Tektronix 011-0059-02) was used to measure current signals. When the inductor was added the external capacitance never exceeded 110 pF, and no attenuator was used. The transient spark circuit with an external capacitor added is labeled TS-C and the circuit with an external capacitor and an inductor added is labeled TS-LC. The original transient spark circuit without additional capacitor or inductor is labeled TS.

The energy delivered to the plasma per pulse, E_p , can be calculated from the measured current I and voltage V waveforms with

$$E_p = \int_T V \times I dt, \quad (1)$$

where the integration period, T , covers the spark current pulse. The discharge power (P) can be obtained by multiplication of the pulse repetition frequency (f) by the energy delivered per pulse, E_p : $P = f \times E_p$. Finally, the energy input density E_d in [J l^{-1}] can be calculated as

$$E_d = P/q \quad (2)$$

where q is the gas flow rate in standard liters per second. Gas flow rates of 0.02 l s^{-1} (1.2 l min^{-1}) were typical in our experiments, controlled by mass flow controllers (Bronkhorst).

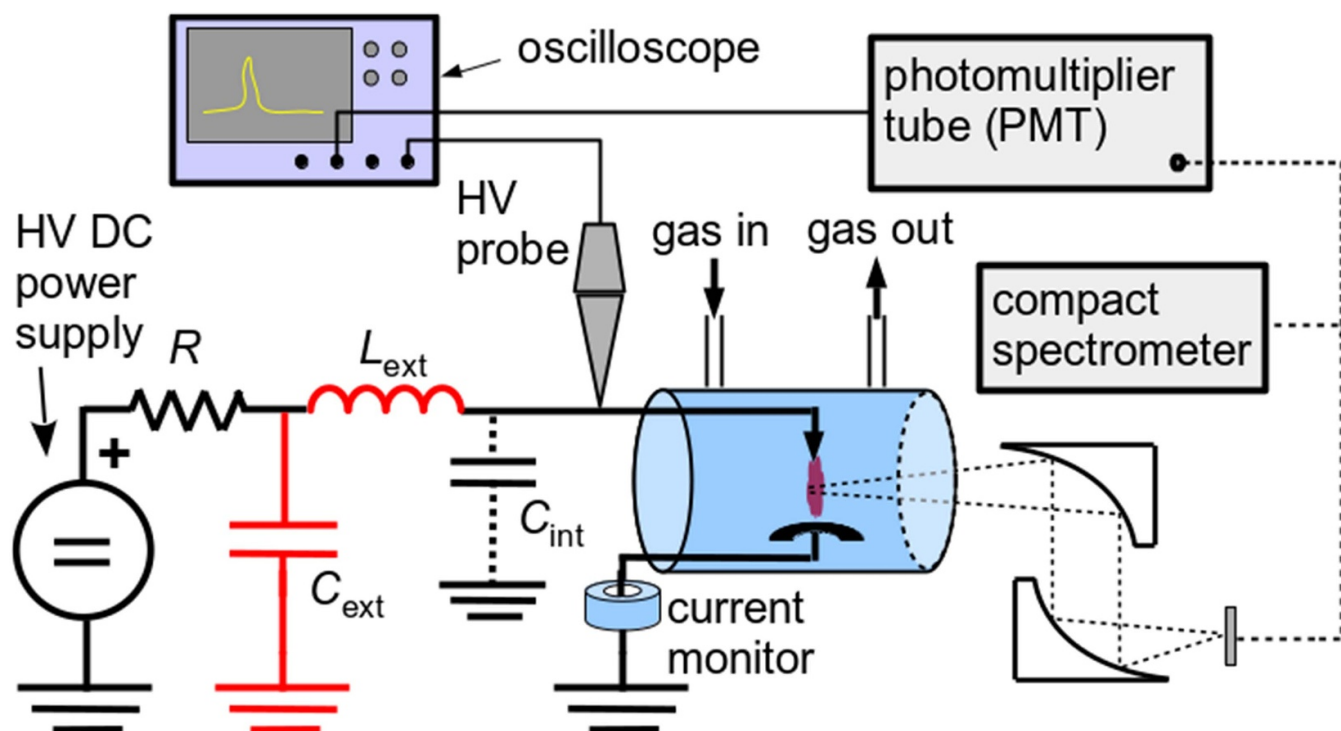


Figure 1. Simplified schematic of the experimental setup, red components of the electrical circuit are optional, used only in some experiments.

Experiments were performed with dry synthetic air (Messer, 99.999% purity; 80% N₂ and 20% O₂). Some additional experiments were performed in an atmosphere of pure oxygen (Linde, 99.99% purity).

The main analytical technique used to determine the composition of the gas after treatment was UV–visible absorption spectroscopy, which is suitable for detection of NO, NO₂, O₃, and HNO₂. A deuterium lamp (Avantes AvaLight-D-S) was used as the light source and absorption spectra were measured with an optical emission spectrometer (Avantes AvaSpec-Mini4096CL). The spectral resolution of this system is 0.5–0.7 nm and spectra in the range 190–650 nm were recorded. The use of multiple absorption cells with different lengths gave a wide dynamic range to the concentrations of RONS that could be detected from a few ppm to more than 1000 ppm. Cuvettes with lengths from 8.5 to 75 cm were used; the longest absorption path, 150 cm, was achieved using a mirror to make a double pass through the 75 cm cuvette.

The second technique used for analysis of plasma treated gas was infrared (IR) absorption spectroscopy, which is more versatile than UV–visible spectroscopy, because more compounds can be found in IR spectra. HNO₃, N₂O, CO, CO₂ and almost all volatile hydrocarbons can be detected in IR spectra in addition to NO, NO₂, HNO₂ and O₃, which are also detectable in the UV–visible region. A Fourier transform infrared (FT-IR) spectrophotometer (Shimadzu IRAffinity-1S) was used with a wavenumber range of 7800–350 cm⁻¹ and a nominal spectral resolution of 1 cm⁻¹.

Both FT-IR and UV–vis absorption techniques are absolute. The concentration of RONS in the gas were obtained by

fitting the measured spectra with calculated ‘synthetic’ spectra. The synthetic FT-IR spectra were calculated from absorption lines for NO, NO₂, H₂O, HNO₃, O₃ and H₂O₂ downloaded from HITRAN database [43]. These absorption lines were convoluted with a Gaussian function to generate synthetic spectra that matched the experimental spectra, which all have a spectral resolution of 1 cm⁻¹. We verified this approach by measurement of NO and NO₂ in commercially obtained gas mixtures of 2000 ppm NO in N₂ and 1000 ppm NO₂ in dry synthetic air (80% N₂ and 20% O₂). As there is no suitable set of absorption lines for HNO₂ in the HITRAN database, we used absorption cross sections downloaded from the supplemental HITRAN database [44] and convoluted them with our spectral resolution.

A similar approach was used to calculate synthetic UV–visible spectra; absorption cross sections of NO, NO₂, HNO₂, HNO₃, N₂O₄, O₃ and H₂O₂ were downloaded from the MPI-Mainz UV/VIS spectral atlas [45]. Again, these absorption cross sections were convoluted to match the spectral resolution of our spectrometer, keeping the area under the curve constant. This approach was again verified by measurement of NO and NO₂ concentrations in commercial gas mixtures with 2000 ppm of NO and 1000 ppm of NO₂.

Emission spectra of spark discharges were taken in addition to the gas absorption measurements. A two-channel compact emission spectrometer (Ocean Optics SD2000) with a 200–1100 nm range and resolution of 0.6–1.2 nm was used to record time-integrated spectra over this broad spectral region. Time resolved measurements of the emission intensity were made with a photomultiplier tube (PMT) with a rise time of

2.2 ns (Hamamatsu H955). In this experiment the evolution in time of specific spectral ranges can be measured with the PMT by inserting bandpass interference filters into the optical path. The PMT module signal was recorded using the oscilloscope.

3. Results and discussion

In this section we present our results from the experimental study of transient spark discharges. We describe transient spark discharge behavior in air generated without any additional capacitor or inductor in section 3.1. The influence of an additional external capacitor is presented in section 3.2. Results obtained by generating transient spark discharges with both an additional capacitor and an inductor are shown in section 3.3. In all three of these sections the electrical characteristics of the transient spark discharges are presented first before a discussion of the chemistry observed, with a focus on the generation of nitrogen oxides.

3.1. Transient spark without additional capacitor and inductor

3.1.1. Electrical characteristics. Figure 2 shows typical waveforms of a transient spark discharge averaged over 128 shots. The discharge is initiated by a streamer creating a channel of ions and electrons between the electrodes. The small current associated with the streamer is just visible in figure 2 at approximately 40 ns before the start of the main current pulse. The energy delivered per pulse depends on the value of the capacitance at the powered electrode. In figure 2 the energy delivered to the plasma per pulse E_p (~ 1 mJ) is limited by the low value of C_{int} (only ~ 25 pF).

In the transient spark the plasma decays after each spark current pulse because the ballast resistor limits the current delivered to the plasma after the capacitance, C , in the driving circuit is discharged. The potential V on the powered electrode gradually increases as C is recharged by the HV supply through the ballast resistor. When the voltage is high enough a new current pulse, initiated by a new streamer, is formed and this cycle repeats. These transient spark current pulses are thus formed by repetitive charging and discharging of C . Here the capacitance is just the ~ 25 pF internal capacitance of the wire between the limiting resistor and the powered electrode, C_{int} .

Figure 3 shows a series of transient spark discharges (black curve). The repetition frequency f of the transient spark process is given by the equation

$$f = \frac{1}{RC \times \ln\left(\frac{V_{\text{in}}}{V_{\text{in}} - V_{\text{BR}}}\right)}, \quad (3)$$

and can be controlled by the input high voltage V_{in} . In this equation it is assumed that the input voltage, V_{in} , and breakdown voltage, V_{BR} , are constant, and that the capacitance C is charged through the ballast resistor R . Figure 3 also shows a voltage waveform, in red, typical of unstable GD behavior that is discussed below.

Figure 4 shows the experimentally determined relationship between transient spark discharge frequency and input voltage,

V_{in} . As expected from equation (3) the frequency increases as the input high voltage rises. The increase in the pulse repetition frequency increases the mean discharge current, I_{mean} , and the average energy density delivered by the transient spark discharge, which are both also shown in figure 4 as a function of the high voltage input, V_{in} . Energy density, E_d , is the energy supplied per liter of input gas.

The current that passes through the ballast resistor after each transient spark when the capacitor has discharged depends on the applied voltage and the resistance of the ballast resistor. As the voltage applied is increased, the current increases and when this current is high enough a glow-type discharge can form. When the mean current, I_{mean} , reaches approximately 1.5 mA in our system, the transient spark discharge tends to transform into an unstable high pressure GD (figure 3, red curve). As the voltage is increased further, a stable GD without transient sparks is typically established in our system with I_{mean} above ~ 2 mA, which typically requires the value of the ballast resistor, R , to be less than 5 M Ω and the applied voltage to be ~ 10 kV or more.

3.1.2. Generation of nitrogen oxides. Figure 5 shows an example of a UV–visible absorption spectrum; the two dominant products detected with dry air were NO and NO₂. At low input energy densities, O₃ signals were also observed, as visible in figure 5. Traces of HNO₂ lines were also observed near 350 nm in some spectra, but this signal was barely above the noise and indicated a maximum concentration of 10 ppm HNO₂; no HNO₂ signal is visible in the example spectrum shown in figure 5. Other possible products which do not appear in the UV–visible spectrum, such as N₂O and HNO₃, were not clearly identified in IR spectra taken. As noted above, the IR spectrometer is sensitive to more molecules than the UV–visible measurements and so IR spectrum measurements were made to look for other potential product molecules.

Figure 6 shows the concentrations of NO, NO₂ and O₃ calculated from the UV–visible spectra as a function of energy density, E_d . Each point shown was calculated from multiple measurements made with the same mean discharge current. For each set of measurements at a particular mean discharge current, the average and standard deviation of each chemical concentration was calculated from at least 8 spectra. Similarly, the average and standard deviation of the energy density at each mean discharge current was calculated from electrical measurements and the gas flow rate. The error bars in figure 6 indicate the average plus or minus one standard deviation.

The concentration of O₃ decreased rapidly with increasing input energy density from ~ 10 ppm at ~ 80 J l⁻¹ to below 1 ppm at ~ 120 J l⁻¹; the O₃ concentration is shown on the right-hand vertical axis of figure 6. At low energy densities the concentration of NO₂ increases slowly as the input energy density increases, but above ~ 150 J l⁻¹ the concentration of NO₂ starts to decline. By contrast, the NO concentration grows as the energy density increases up to ~ 220 J l⁻¹. At higher input energy densities above 220 J l⁻¹, with this driving circuit, an unstable GD is formed and the concentration of

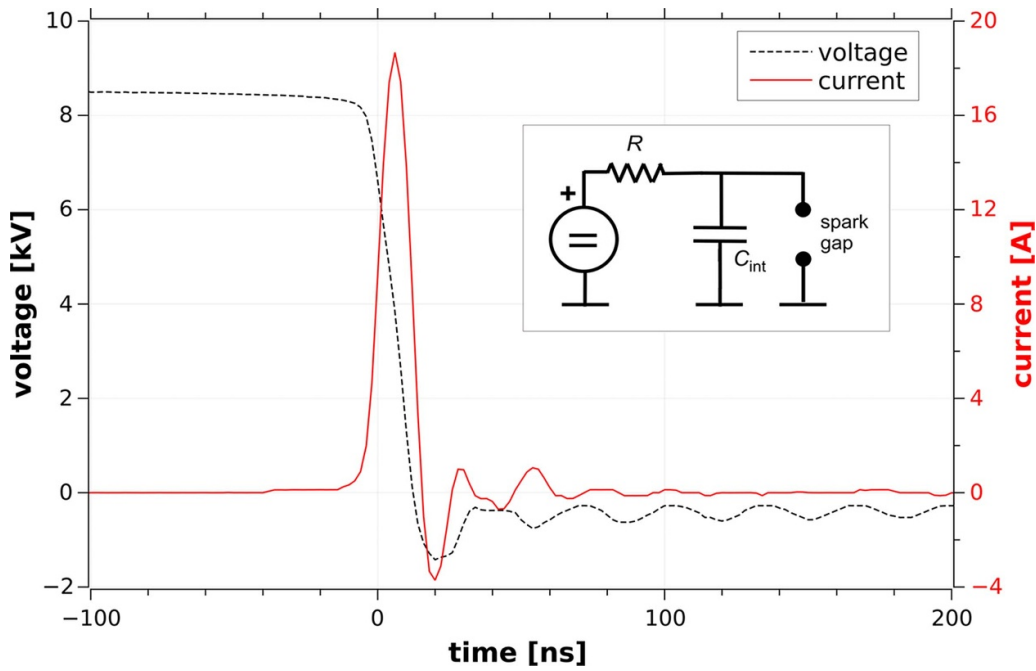


Figure 2. Typical waveforms of transient spark discharges without additional circuit components (TS), $C_{int} \sim 25$ pF, $R = 8$ M Ω , 8 mm gap, short time scale with focus on spark current pulse and voltage drop during the breakdown; the inset shows a simplified schematic diagram of the TS driving circuit.

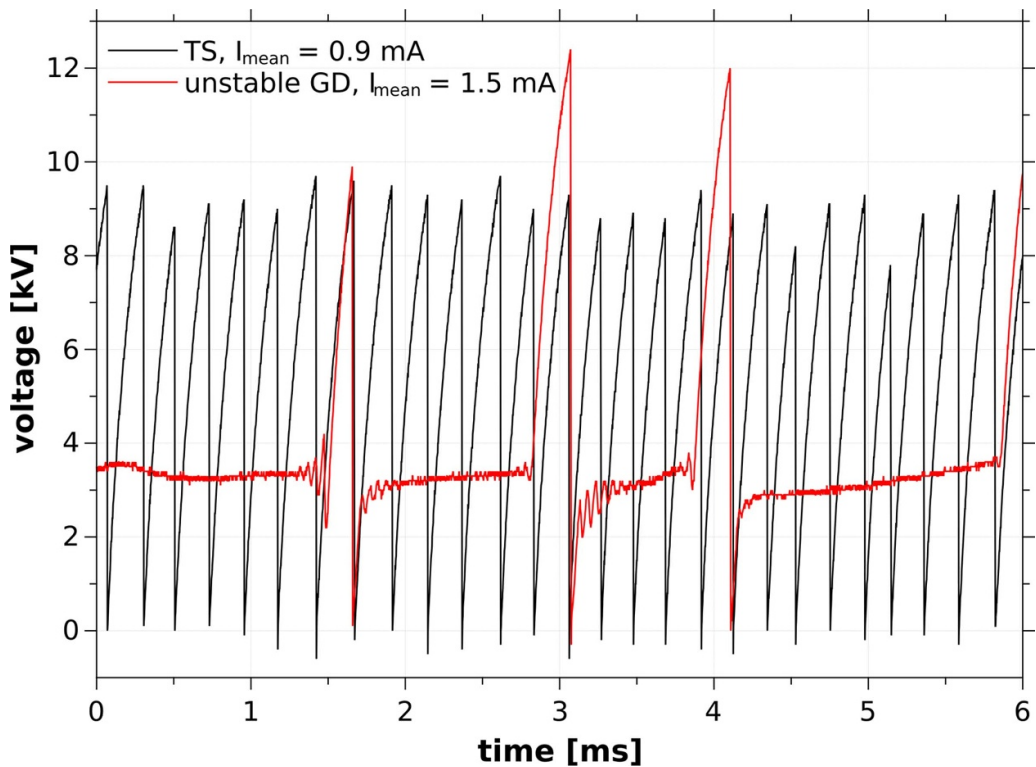


Figure 3. Typical voltage waveforms of transient spark discharges without additional circuit components (TS), $C_{int} \sim 25$ pF, $R = 9.4$ M Ω , 10 mm gap, long time scale, comparison of TS ($I_{mean} = 0.9$ mA), with unstable glow discharge (GD).

NO remains almost constant, or even decreases, as the energy density increases.

The results shown in figure 6 show that the efficiency of NO production by GD is lower than by transient spark

discharge. It might be surprising that the GD formation of NO is less efficient than transient spark NO formation. Two factors need to be considered in relation to this change in NO production efficiency: the different characteristics of

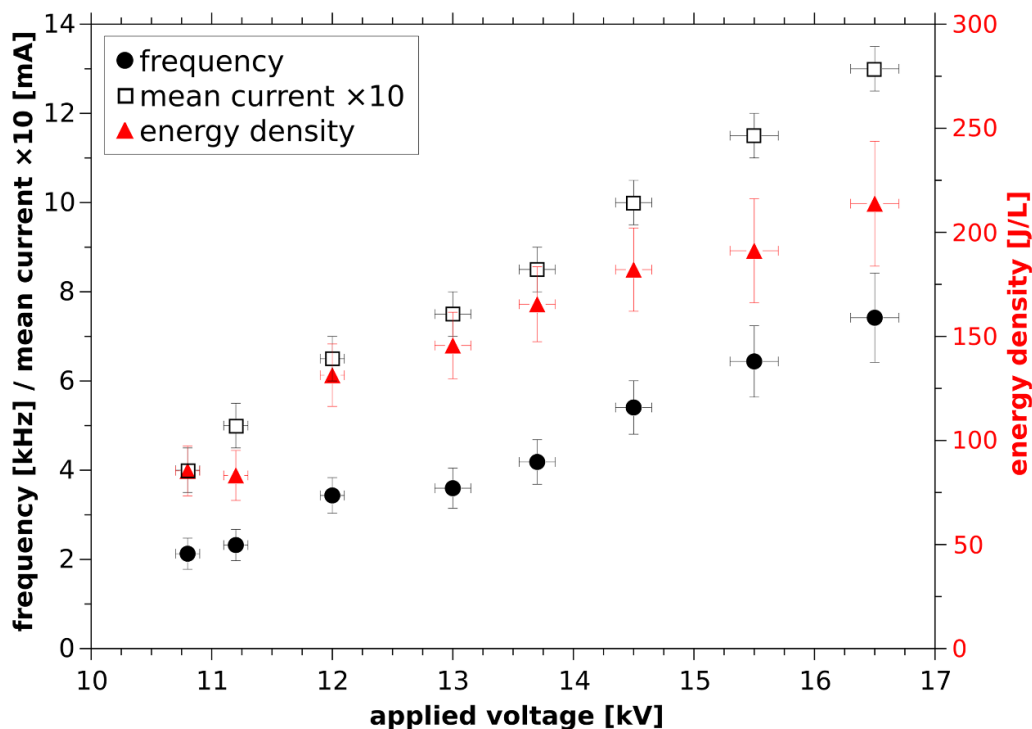


Figure 4. The transient spark discharge electrical characteristics (frequency, mean current, and energy input density) as functions of the applied generator voltage, $R = 9.4 \text{ M}\Omega$, $C_{\text{int}} \sim 25 \text{ pF}$, 10 mm gap; transient spark with no additional capacitor or inductor (TS).

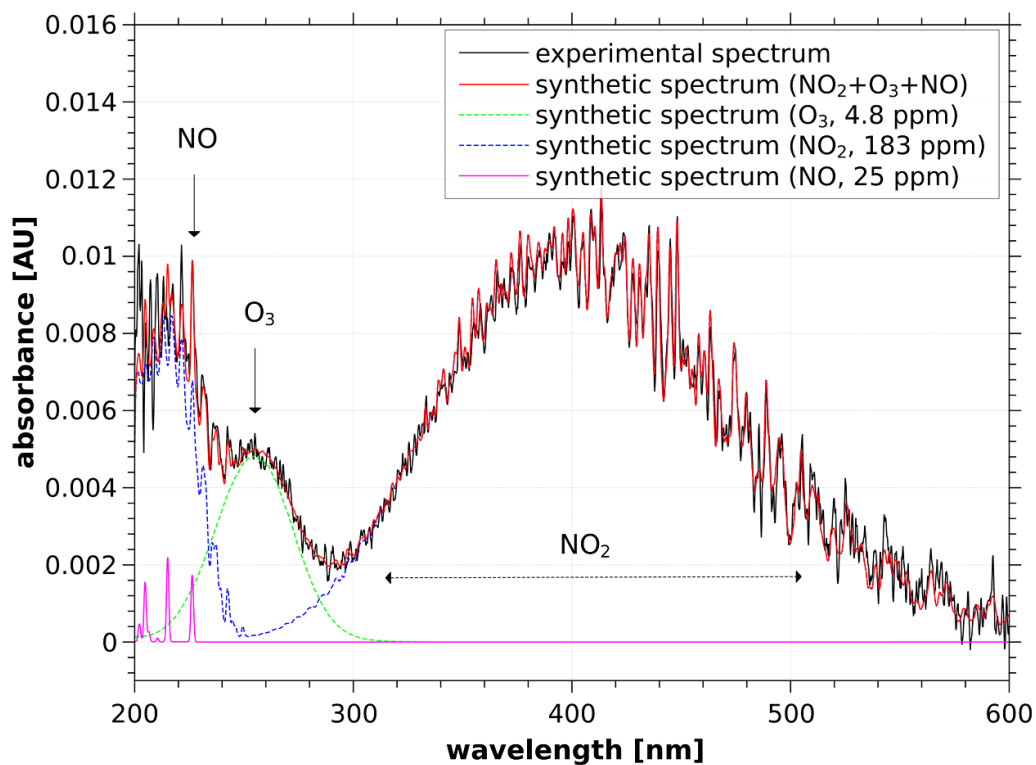


Figure 5. UV-vis absorption spectrum: experiment, air treated by transient spark discharges without additional capacitor or inductor (TS), $E_d \sim 90 \text{ J l}^{-1}$, and synthetic spectra of O_3 , NO, NO_2 and the synthetic combined spectrum of all three components. The absorption path length in this measurement was 8.5 cm.

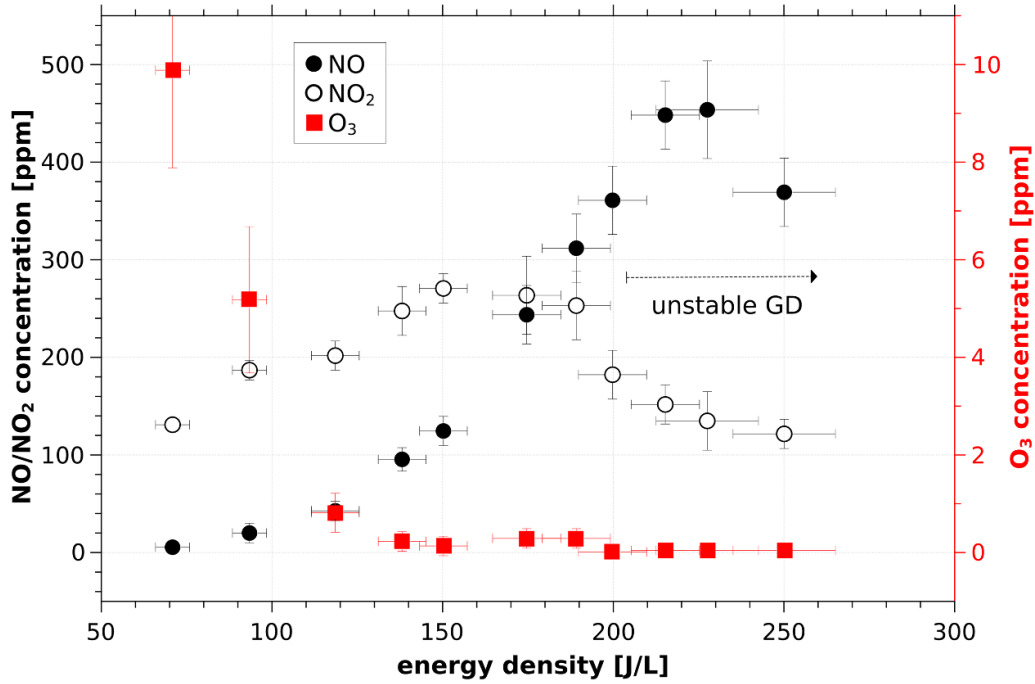
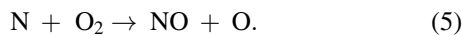


Figure 6. Generation of NO, NO₂ and O₃ by transient spark discharge without additional capacitor and inductor (TS), $R = 9.4 \text{ M}\Omega$. At energy density $E_d > 200 \text{ J l}^{-1}$ the discharge is an unstable glow discharge (GD) of the type shown with the red waveform in figure 3. The applied voltage was varied between ~ 10.5 and 17 kV in these measurements.

transient spark and GDs, and the likely mechanism of NO formation.

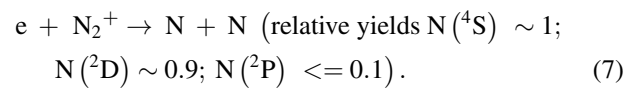
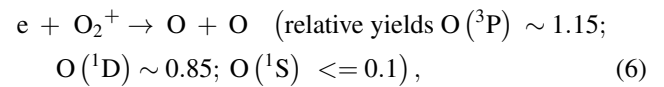
The gas inside the GD plasma channel is permanently heated to temperatures above 2000 K by a continuous current [46]. In the transient spark discharge the average gas temperature is lower, but higher temperatures ($>3000 \text{ K}$) can be achieved during the short spark phase [40]. Under these high temperature conditions, NO generation via the thermal Zeldovich mechanism is possible in both discharges. In this mechanism, NO generation proceeds via reactions:



The rate coefficient of the reaction (5) with N atoms is six orders of magnitude higher at 2000 K than the rate coefficient of reaction (4) [47]. High temperature is needed, because N₂ molecules must be in high vibrational state to lead to NO production by the reaction (4), which can be thus considered as limiting factor for NO generation by thermal Zeldovich mechanism. The vibrational excitation of N₂ in NTP can help overcome the reaction energy barrier in reaction (4) and can thus significantly enhance the production of NO [48].

Next, the initiation of NO generation by these reactions requires formation of some O or N atoms, for example by thermal decomposition of N₂ and O₂ molecules. In NTP, there are other reactions which can enhance generation of O and N atoms. For O and N atom generation, it is necessary to consider the different characteristics of the transient spark and GDs.

In GDs, the plasma is closer to thermal equilibrium conditions and much weaker intensities of atomic emission lines are observed compared to the strength of atomic lines in transient spark discharges [40]. In transient spark discharges a high degree of ionization is achieved, with electron densities above $\sim 10^{17} \text{ cm}^{-3}$ in the short discharge [41]. By contrast, electron densities are typically only $\sim 10^{12} \text{ cm}^{-3}$ in continuous GD [46]. The high degree of ionization in transient spark discharges results in higher concentrations of N and O atoms in ground and excited states formed in dissociative electron-ion recombination reactions [47]:



Reactions (4) and (5) are much faster if one of the reactants is in an excited state [47] and a significant fraction of the atomic products formed in reactions (6) and (7) are formed in electronically excited states; O(¹D and ¹S) and N(²D and ²P). Thus, from this consideration of the non-thermal Zeldovich mechanism, the rate of NO production in transient spark discharges may be higher than the rate in a GD due to higher rates of N and O atom production in the transient spark with a significant fraction of excited state atoms. However, we must emphasize that additional research is needed to prove this hypothesis, and chemical kinetic modeling of both discharges.

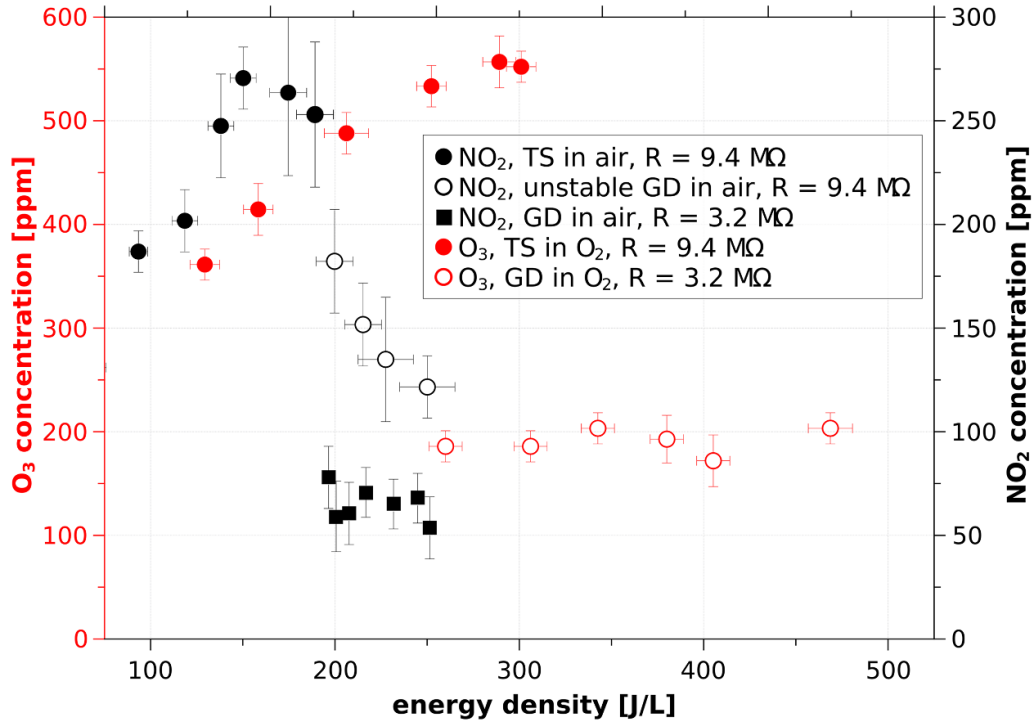
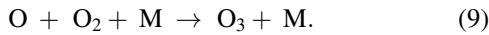
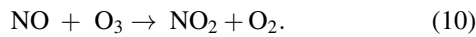


Figure 7. Comparison of O₃ concentration produced by transient spark and glow discharges in O₂ gas with NO₂ generated in synthetic air.

In the transient spark, NO production stops after the spark current pulse when the gas cools down. Available O atoms start to oxidize NO to NO₂ and generate ozone O₃ by reactions



The rate coefficient of the reaction (8) is higher than the rate coefficient of the reaction (9), but there are probably much more O₂ molecules to react with O than NO molecules. Therefore, it is questionable which of these reactions is the major sink of O atoms. Based on preliminary results from chemical kinetic modeling [49], the formation of O₃ is more important. Subsequently, O₃ oxidizes NO to NO₂:



Practically all O₃ is consumed in reaction (10) if there is enough NO. Therefore, in figure 6, O₃ is only observed at very low energy densities, E_d , when the concentration of NO generated shortly after the spark current pulse is low. As the concentration of NO increases, the O₃ is used up in reaction (10) as it converts NO to NO₂.

The generation of NO₂ is even more influenced by the transition from transient spark to unstable GD than the generation of NO. There is a clear decrease in NO₂ as the energy density rises above $\sim 190 \text{ J l}^{-1}$ visible in figure 6. The lower production efficiency of NO₂ in GDs can also be linked to the efficiency of O₃ production, which should be lower in GD than in transient spark.

To test this hypothesis that the concentration of NO₂ mainly depends on the quantity of O₃ produced in the discharge, the formation of O₃ in the transient spark and GD was investigated by running these discharges in artificial air and in oxygen input gas alone without nitrogen present. Transient spark discharges were generated with the unmodified driving circuit to obtain the data shown in figure 6 with an external ballast resistor $R = 9.4 \text{ M}\Omega$. Stable GD was generated with the same driving circuit, but with the value of R reduced to $3.2 \text{ M}\Omega$. In oxygen, the discharge generates O₃, but without nitrogen there is no NO and the O₃ generated cannot be depleted in favor of NO₂ formation. Thus, the concentration of O₃ generated by the different discharges with oxygen input gas can be measured and compared with the NO₂ generated using artificial air input gas. Note that with oxygen input gas, the only significant gaseous product was O₃.

Figure 7 shows a comparison of O₃ and NO₂ formed in transient spark discharge with oxygen and artificial air feed gases. The red points show O₃ concentrations from transient spark in oxygen with the scale shown on lefthand axis. The black points show NO₂ concentrations from discharges in artificial air with the scale shown on the righthand axis. The ratio between the scales on the lefthand and righthand sides of the figure is an arbitrary factor of 2. The factor of 2 was chosen to aid the comparison of the O₃ and NO₂ concentration trends. In the case of artificial air, black open circle points are also shown for unstable GD with E_d above $\sim 190 \text{ J l}^{-1}$. Note that the NO₂ data for transient spark discharges in artificial air in figure 7 are the same as the data for NO₂ concentration shown in figure 6.

The results shown in figure 7 show that there are some similarities between the trends in the concentrations of O₃ and NO₂. At low energy densities in the transient spark the

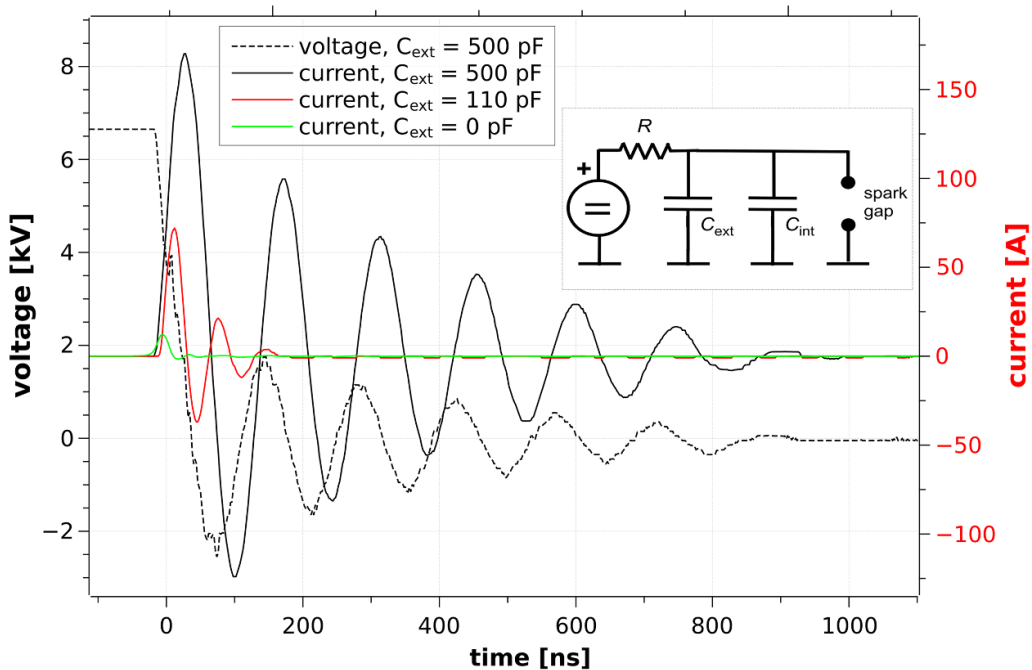


Figure 8. Influence of C_{ext} on transient spark current pulses, $R \sim 9.4 \text{ M}\Omega$, $C_{\text{int}} \sim 25 \text{ pF}$; the inset shows a simplified schematic diagram of the TS-C driving circuit.

concentrations of both O_3 and NO_2 rise with increasing E_d . In the unstable GD in air, the concentration of NO_2 decreases, probably due to the smaller amounts of O_3 produced. Lower production rates of O_3 by unstable GD compared to transient spark production rates can be explained by the continuous high temperature in the GD plasma channel, where the temperature exceeds 2000 K. O_3 is thermally unstable under these conditions and could be produced only by diffusion of O atoms to the colder area of the reactor. With transient no decrease of O_3 concentration at higher spark running in oxygen, the unstable GD was not observed and therefore also input energy densities.

The O_3 concentration generated by transient spark discharges in oxygen is relatively high; 400–550 ppm. These concentrations exceed the concentrations of NO_2 generated with synthetic air. Indeed, it is not correct to compare these concentrations quantitatively, because they were obtained with different input gases and, for example, a partial pressure of oxygen is five times greater in oxygen than in dry air. We note, however, that the O_3 concentrations observed with oxygen as the input gas are of the order of magnitude that we would expect if all NO_2 is formed by the reaction of O_3 with NO . Next, we must emphasize that here we have only presented several plasma induced chemical reactions, focusing on major stable products, NO , NO_2 and O_3 , but there are hundreds of other reactions in air plasmas involving tens of other short lived radicals, [50] electrons and ions.

3.2. Transient spark with additional capacitor (TS-C)

The first modification to the driving circuit is described here; the addition of an external capacitor, C_{ext} .

It is clear from the previous section that (i) transition from transient spark to GD leads to a reduction in the generation efficiency of both NO and NO_2 , which is not desirable, and (ii) increasing the mean discharge current and the input energy density changes the discharge from a transient spark discharge to an unstable GD, as visible in figure 3. One way to prevent the discharge from changing to a GD is to increase the value of the ballast resistor, R , but even with $R \approx 10 \text{ M}\Omega$ an unstable GD is formed with discharge currents of 1.5 mA or more. Further increases of R are not useful because the energy losses on the external resistor become too high. Even for $R = 6.6 \text{ M}\Omega$, the power dissipated in the external resistor exceeds the power input to the plasma for mean transient spark discharge currents above 0.6 mA [39].

The results presented here show an external capacitor, C_{ext} , in the range 50–500 pF added to the driving circuit (TS-C), enables higher energy densities to be delivered by transient spark discharges before the transition to GD.

3.2.1. Electrical characteristics. Figure 8 shows current waveforms of transient spark discharges with an additional external capacitor, C_{ext} , in the driving circuit (TS-C). The TS-C peak current, as well as energy per pulse are higher compared to similar values for TS without an additional capacitor. The reason for this increase with the TS-C driving circuit can, of course, be attributed to higher capacitance being discharged in each pulse. It is also clear from figure 8 that as the value of the capacitance discharged increases, the current oscillations after the initial current peak are stronger and more prolonged.

The damped oscillations appear to be due to RLC oscillations where C is the total capacitance, $C_{\text{ext}} + C_{\text{int}}$, L is the intrinsic inductance of the plasma, L_{int} , and R is the resistance

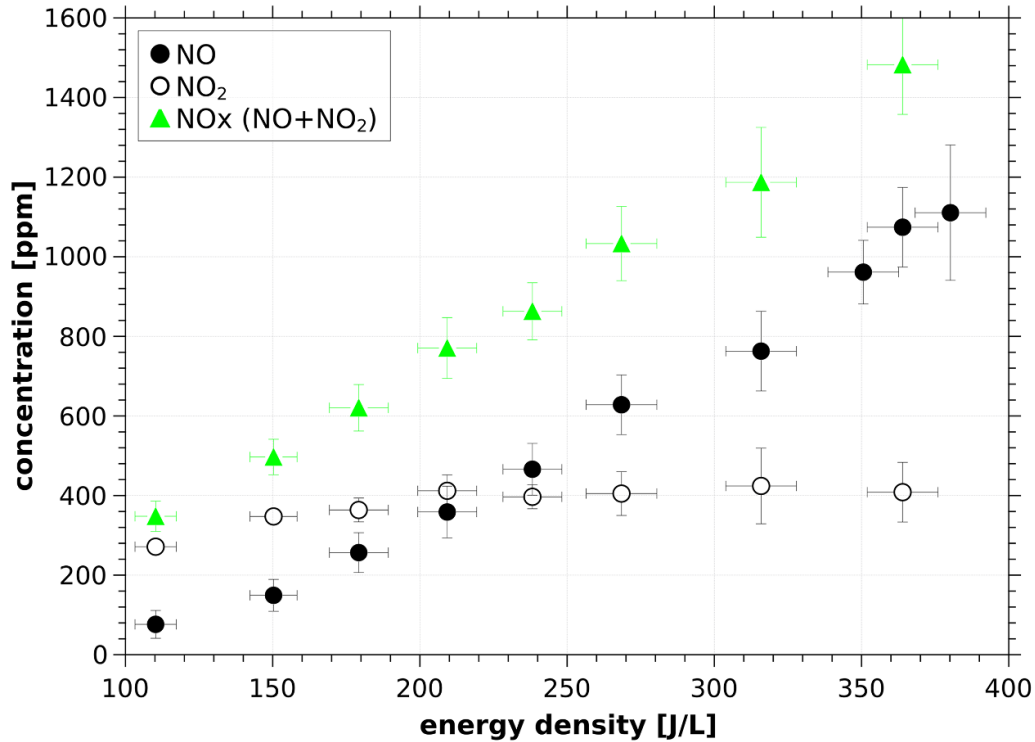


Figure 9. Generation of NO and NO₂ by transient spark discharge with additional external capacitor $C_{\text{ext}} = 50$ pF in the driving circuit.

of the plasma, R_p . Without the additional external capacitor these oscillations are damped heavily by the resistance of the plasma, but with the increased capacitance from C_{ext} and the large initial current peak, the plasma generated has a lower resistance and RLC oscillations are only lightly damped. In reality the situation is more complicated, because during each discharge pulse the inductance and resistance of the plasma change with time. Consideration of these phenomena is beyond the scope of this work and is discussed elsewhere [42].

The total capacitance, C , of the electrical driving circuit was increased from the internal capacitance of ~ 25 pF by adding capacitors of 50 pF–500 pF; $C = C_{\text{int}} + C_{\text{ext}}$. The increase in C increased the energy per pulse, nominally $1/2 CV^2$, but also caused a decrease in the discharge pulse frequency, nominally proportional to $1/RC$ as predicted by equation (3). Thus, the addition of an external capacitor gives an increase in energy per pulse proportional to C which is balanced by a decrease in pulse frequency inversely proportional to C and the total input energy density does not change significantly compared to transient spark without an external capacitor. With the additional capacitor, C_{ext} , however, it was possible to decrease R from 9.4 M Ω to 2–3 M Ω without the plasma becoming a GD. This reduction in R increased the repetition frequency, again proportional to $1/RC$ from equation (3), which enabled the energy density to be increased. The energy density delivered to the gas can be increased up to at least ~ 400 J l⁻¹ without transition to either unstable or stable GD, by adding capacitance to the driving circuit and consequently by reducing R .

In the transient spark discharge without additional capacitor C_{ext} , R cannot be reduced because high R values limit the current and prevent the transient spark discharge from changing to a GD. With an additional capacitor, the resistance of the ballast resistor can be reduced and the transient spark discharge does not change to a GD. There are two major effects that could explain additional capacitance preventing the transition to GD. First, there will be stronger oscillations in the potential over the spark gap (figure 8). The GD needs a stable voltage of 2–3 kV to be maintained so due to the voltage oscillations, there is a delay between the end of the spark pulse and initiation of a GD. It appears that during this delay before the GD can start, the plasma channel conductivity decreases. Second, with more energy released in each pulse with the additional capacitance, there will be more hydrodynamic distortion. Hydrodynamic instabilities may cause the conductive electron ion channel to be disrupted during the period with oscillations. Disruption of the conductive channel will prevent GD formation.

3.2.2. Generation of nitrogen oxides. In figure 9, the concentrations of NO and NO₂ formed as functions of energy density are shown for driving circuit with additional capacitor $C_{\text{ext}} = 50$ pF. From 100 J l⁻¹ to 200 J l⁻¹, the concentration of NO₂ increases from ~ 300 ppm to ~ 400 ppm, but above ~ 210 J l⁻¹, it is constant within the experimental uncertainty. By contrast, the NO concentration grows almost linearly as energy density increases, up to ~ 1100 ppm at

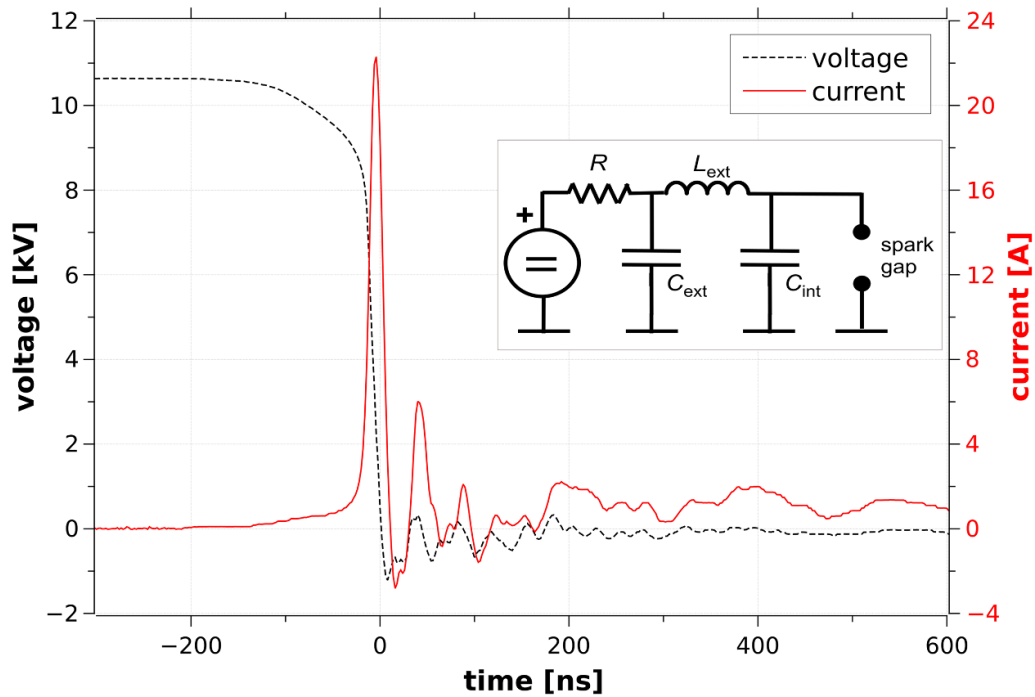


Figure 10. Transient spark voltage and current waveforms with additional $C_{\text{ext}} = 50$ pF and $L_{\text{ext}} = 0.73$ mH (TS-LC), gap 10 mm, $R \sim 3.2$ M Ω , short time scale; the inset shows a simplified schematic diagram of the TS-LC driving circuit.

~ 380 J l^{-1} . Therefore, at high energy densities, higher NO and NO₂ concentrations are generated in TS-C (with the additional capacitor, C_{ext}) shown in figure 9 than for the TS discharge (without an additional external capacitor) shown in figure 6. This improved performance with the additional capacitor appears to be because discharge does not transition into an unstable or stable GD at higher input energy densities.

A striking result in figure 9 is that the additional capacitor significantly improves the efficiency of NO₂ generation at all energy densities compared to the transient spark without capacitor shown in figure 6. For example, the peak NO₂ concentration in the transient spark without capacitor at 150 J l^{-1} was ~ 270 ppm, but with the additional capacitor it is ~ 350 ppm. Higher NO₂ concentrations are particularly evident for energy densities above ~ 180 J l^{-1} , which appears to be due to the lack of GD mode with the additional capacitor. The increased NO₂ generation at all energy densities with the additional capacitor could be because the TS-C current pulses are stronger, with more energy per pulse. The pulses cause stronger hydrodynamic distortion associated with the TS-C current pulses, which are expected to give faster mixing of the plasma channel with the surrounding air and, hence, faster cooling. Improved cooling will enhance O₃ generation and hence increase NO₂ production assuming the dominant mechanism of NO₂ production is the oxidation of NO by O₃ as discussed above.

3.3. Transient spark with additional external capacitor and inductor added (TS-LC)

The goal of this research is to improve transient spark energy efficiency, while keeping, or even improving its chemical reactivity. The additional external capacitor enabled us to

decrease the ballast resistor from 10 down to 3 M Ω , which reduces the energy losses in the circuit. In this section the performance of the transient spark with an external capacitor and an inductor added to the driving circuit is described.

3.3.1. Electrical characteristics. Figure 10 shows characteristic short timescale waveforms of the transient spark with an additional capacitor and inductor (TS-LC); the values of the additional capacitance and inductance are $C_{\text{ext}} = 50$ pF and $L_{\text{ext}} = 0.73$ mH. In figure 10 the maximum current is 22 A, but without inductor present (TS-C, $C_{\text{ext}} = 50$ pF) the current pulses are stronger, and the maximum current is above 30 A. Thus, the presence of L_{ext} in the circuit has a significant effect on the initial TS-LC current peak amplitude and duration, which is similar to the transient spark current pulse without capacitor or inductor shown in figure 2. The additional inductor L_{ext} , however, increases the length of the discharge to $\sim 5\text{--}6$ μs .

Figure 11 shows voltage and current waveforms of the TS-LC over a longer time scale than figure 10. The addition of inductor, L_{ext} , causes voltage and current oscillations, and the energy stored in the capacitance, $C = C_{\text{int}} + C_{\text{ext}}$, is delivered through the gap gradually over ~ 5 μs . It is clear in figure 8 that there are also oscillations after the initial current peak in TS-C, which are due to the intrinsic inductance of the plasma. These TS-C oscillations shown in figure 8, however, are about ten times higher in frequency than the oscillations of TS-LC. Furthermore, with the additional inductance, L_{ext} , the oscillations in figure 11 are not simple damped sinusoidal oscillations. In the first 5 μs after breakdown the voltage oscillations are influenced by the low resistance (high

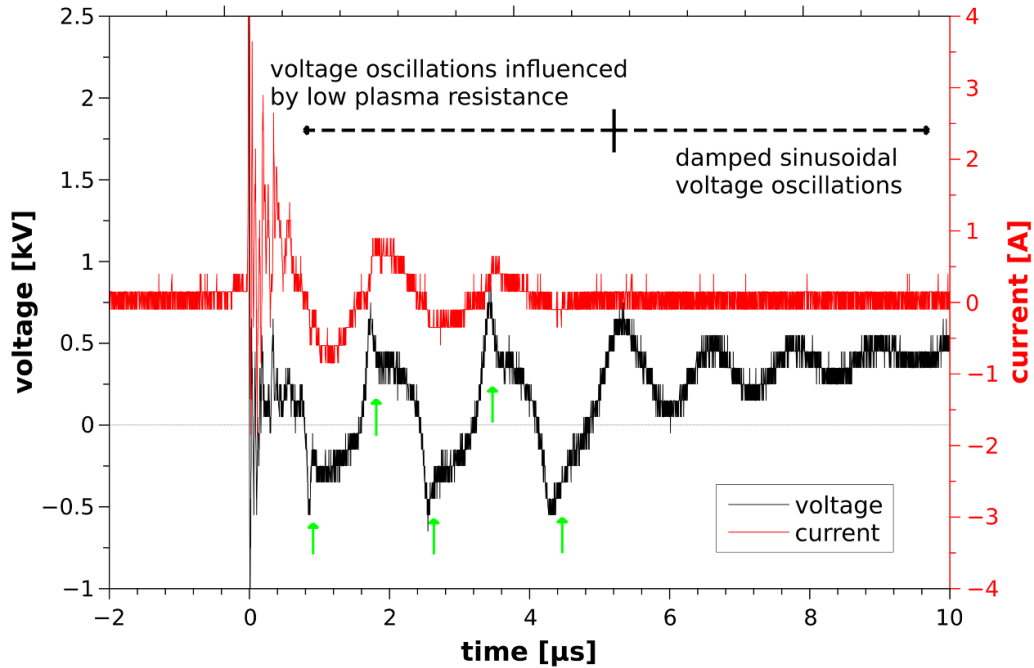


Figure 11. Transient spark voltage and current waveforms with additional $C_{\text{ext}} = 50$ pF and $L_{\text{ext}} = 0.73$ mH (TS-LC), $R \sim 3.2$ M Ω , longer time scale; green arrows indicate decreases of voltage (absolute value) associated with plasma ‘re-ignition’.

conductivity) of the plasma channel. It appears that when the voltage switches polarity, the magnitude of the voltage increases to a certain value needed to ‘re-ignite’ the plasma. After the plasma is ‘re-ignited’, the magnitude of the voltage decreases due to the increased plasma conductivity and so the shape of the voltage oscillations differs from damped sinusoidal oscillations. Times where the voltage decreases after ‘re-ignition’ are indicated by green arrows in figure 11. After several ‘re-ignitions’, the plasma does not re-ignite at approximately $5 \mu\text{s}$ after breakdown. After $\sim 5 \mu\text{s}$ the electrical energy remaining in the inductor and capacitor is dissipated in damped sinusoidal oscillations and the mean voltage starts to rise as the capacitor is recharged through the ballast resistor.

By contrast, without the additional inductor the oscillations in figure 8 appear to be simple damped sinusoidal oscillations right after the breakdown. In figure 8 the damped oscillations in the current are shown because the plasma is ignited, but in figure 11 after $\sim 5 \mu\text{s}$ the damped oscillations are visible in the voltage, but not the current waveform, because the plasma does not reignite after $\sim 5 \mu\text{s}$.

The extended $5\text{--}6 \mu\text{s}$ length of the discharge after the initial breakdown is confirmed by the emission intensity obtained with the PMT shown in figure 12. Figure 12 shows light emission intensity and discharge current waveforms, averaged over 128 transient spark pulses. The discharge current and emission intensity are in phase; local extremes of the current are associated with local maxima of the emission intensity. This is valid for both total emission intensity (figure 12, red curve, $200\text{--}850$ nm), as well as for the emission between 340 and 360 nm

(figure 12, green curve). Note that the intensities of the emission signals are arbitrary and have been adjusted so that the total emission signal and the filtered $340\text{--}360$ nm signal have similar intensities between 1 and $4 \mu\text{s}$.

Figure 13 shows a time-integrated optical emission spectrum of transient spark generated by driving circuit with an additional inductor and capacitor, L_{ext} and C_{ext} . This spectrum shows that the significant part of the optical signal measured with PMT in the range $340\text{--}360$ nm can be assigned to continuum radiation, emission of the N^+ ion (line at 343.7 nm); and in part to the second positive system (SPS) of N_2 caused by emission from excited molecular nitrogen, $\text{N}_2(\text{C}^3\Pi_u)$. Emission from the SPS of N_2 suggests the presence of high energy of electrons with >10 eV, because the $\text{N}_2(\text{C}^3\Pi_u)$ species are dominantly produced by collision of energetic electrons with N_2 in the ground state [51]. The combination of continuum radiation, N^+ ion emission, and SPS of N_2 in the $340\text{--}360$ nm range makes it difficult to draw conclusions from these measurements. Further study using time-resolved optical emission spectroscopy should help to gain more insight into this issue.

Figure 14 shows three emission spectra generated with different driving circuits; no external capacitance or inductance (TS), additional capacitance only (TS-C), and both additional capacitance and inductance (TS-LC). These emission spectra show that in addition to emission from N^+ and N_2 mentioned above there are multiple emission lines from O^+ and N^{++} , and bands from the first negative system of N_2^+ . The strongest emission line is the N^+ ion line near 500 nm in the emission of

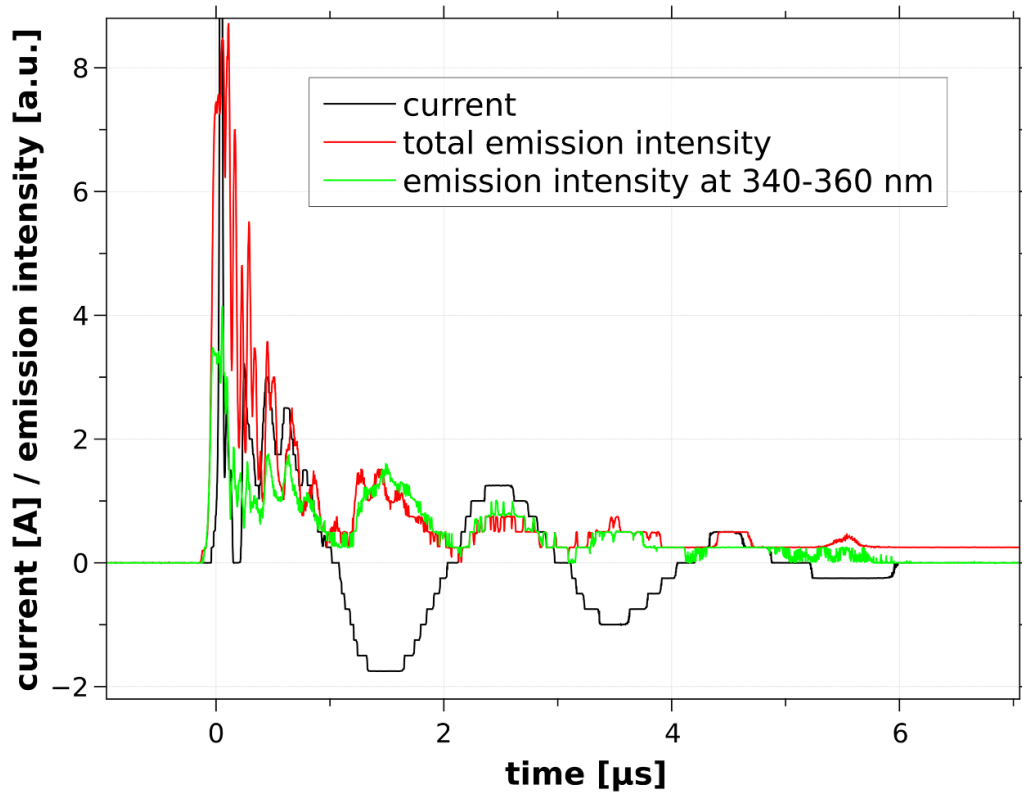


Figure 12. Comparison of TS-LC current waveforms with optical emission intensity measured with a PMT, $C_{\text{ext}} = 110$ pF and $L_{\text{ext}} = 0.73$ mH, gap 10 mm, $R \sim 3.2$ M Ω .

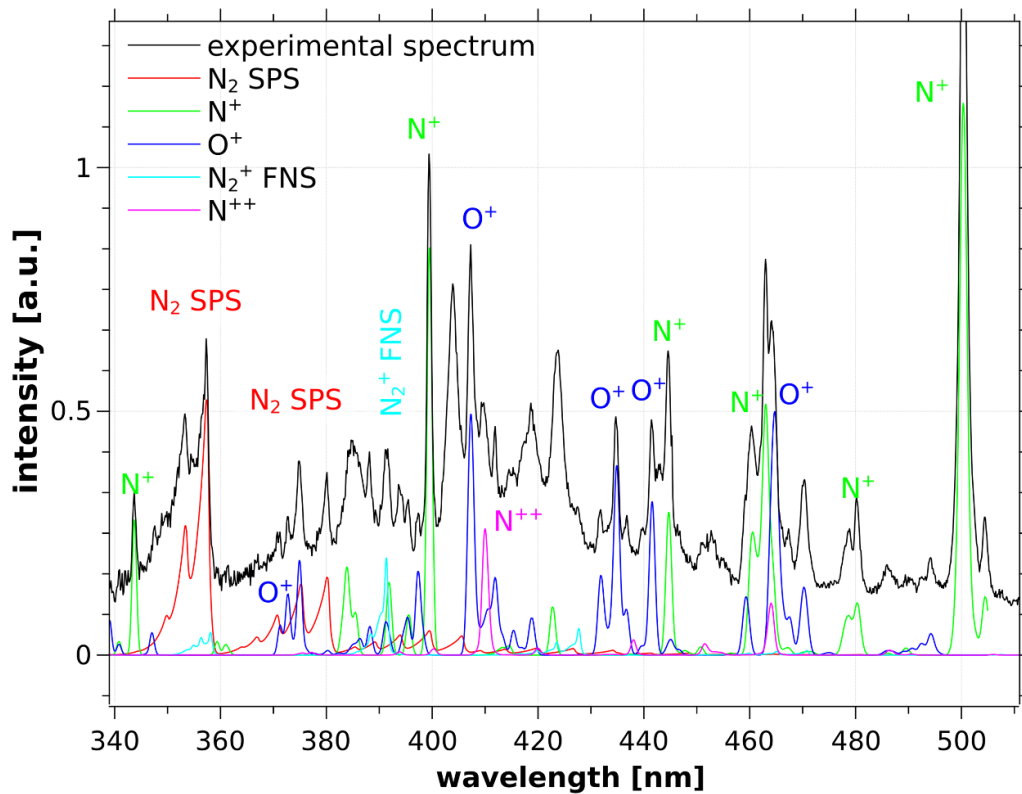


Figure 13. Optical emission spectrum of transient spark, driving circuit with additional $C_{\text{ext}} = 110$ pF and $L_{\text{ext}} = 0.73$ mH, gap 8 mm, $R \sim 3.2$ M Ω .

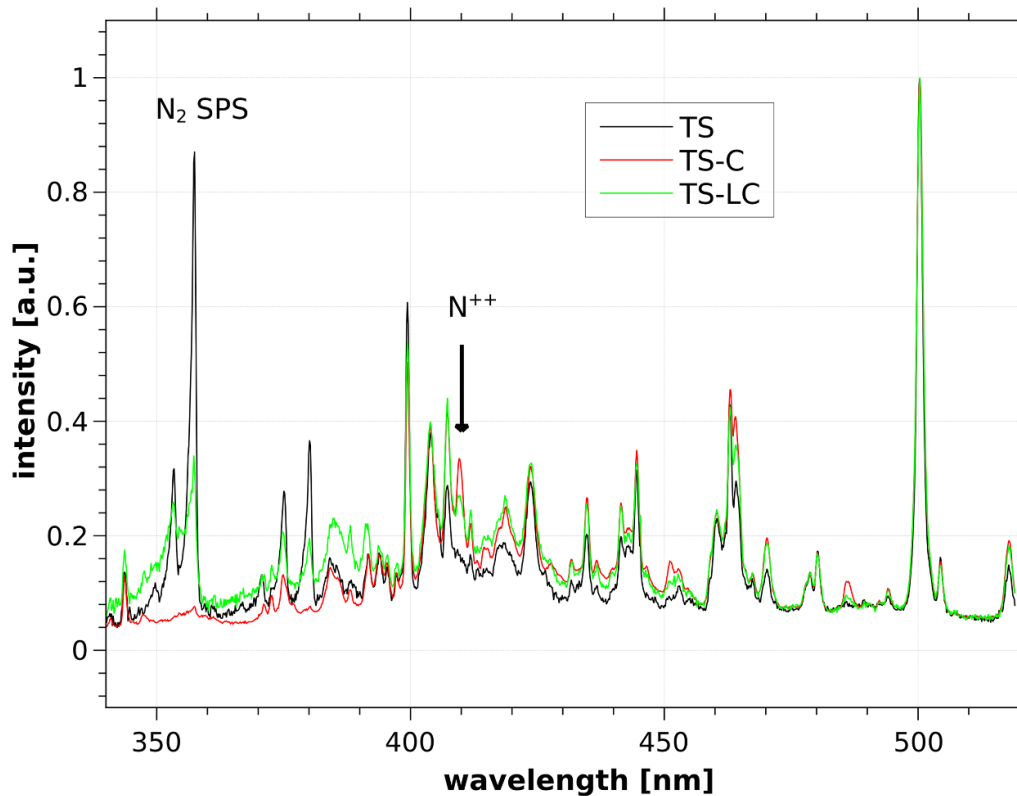


Figure 14. Comparison of normalized optical emission spectra of transient spark generated in three different driving circuits; TS ($R \sim 9.4 \text{ M}\Omega$), TS-C with capacitor added ($C_{\text{ext}} = 110 \text{ pF}$ and $R \sim 3.2 \text{ M}\Omega$) and TS-LC with inductor and capacitor added ($C_{\text{ext}} = 110 \text{ pF}$ and $L_{\text{ext}} = 0.73 \text{ mH}$, $R \sim 3.2 \text{ M}\Omega$), gap 8 mm.

transient spark discharges generated using all three driving circuits. Figure 14 shows the optical emission spectra of transient spark discharges generated with each of these three driving circuits, which are all normalized to the intensity of the strongest N^+ ion line near 500 nm. At first glance, the three spectra are almost identical. Two differences, however, are worth considering.

First, the relative intensity of molecular nitrogen emission (N_2 SPS) is high in transient spark discharges without external C_{ext} and L_{ext} (TS), but is less intense with the additional inductor and capacitor (TS-LC) and it has a very low intensity with the additional capacitor only (TS-C). In our previous work we observed that the emission of the molecular nitrogen is generated mainly during the pre-breakdown streamer phase of the transient spark [40, 52]. Thus, the observed variation of relative N_2 SPS intensity shown on figure 14 could be explained by higher emission intensity during the spark phase compared to the streamer phase in transient spark generated with additional inductor and capacitor, or with capacitor only, which is consistent with higher energy per pulse in these cases.

Secondly, the emission line of N^{++} near 410 nm is almost negligible in the TS spectrum and is the strongest in TS-C. The strength of the N^{++} line indicates that the highest degree of ionization is obtained with the TS-C driving circuit, as might be expected as the TS-C circuit delivers the highest amplitude peak spark current pulses.

3.3.2. Generation of nitrogen oxides. In figure 15, the concentration of NO formed as a function of energy density is shown for several different driving circuits. The striking result is that the NO generation efficiency is significantly increased by a factor of 2–3 with the additional external inductance L_{ext} (0.73 mH) added to the driving electrical circuit. It is interesting that higher NO efficiency generation was not achieved by adding an external capacitor, C_{ext} , but by addition of both a capacitor and an inductor, C_{ext} and L_{ext} . With C_{ext} only, the transient spark current pulses are stronger and there is spectroscopic evidence for a higher degree of ionization and so a higher degree of atomization is expected. Thus, with C_{ext} only, the discharge should produce more N atoms for reaction (7), which is crucial for NO formation.

Another point to consider is that the strongest spark current pulses with the additional capacitor C_{ext} will cause the strongest shock waves and fastest mixing with the surrounding air, leading to faster cooling. The presence of the additional inductor, L_{ext} , in the driving circuit changes the situation significantly; the energy stored in C_{ext} is delivered to the gap gradually over 5–6 μs as shown in figure 11, whereas the other pulses are less than 1 μs long. The length of the pulse is probably responsible for the enhanced NO generation efficiency in the circuit with external capacitor and inductor added. Perhaps the plasma remains hot enough to favor NO formation for a longer period in the extended pulse.

Figure 16 shows that the generation of NO_2 was not enhanced by addition of the inductor, L_{ext} , to the circuit and

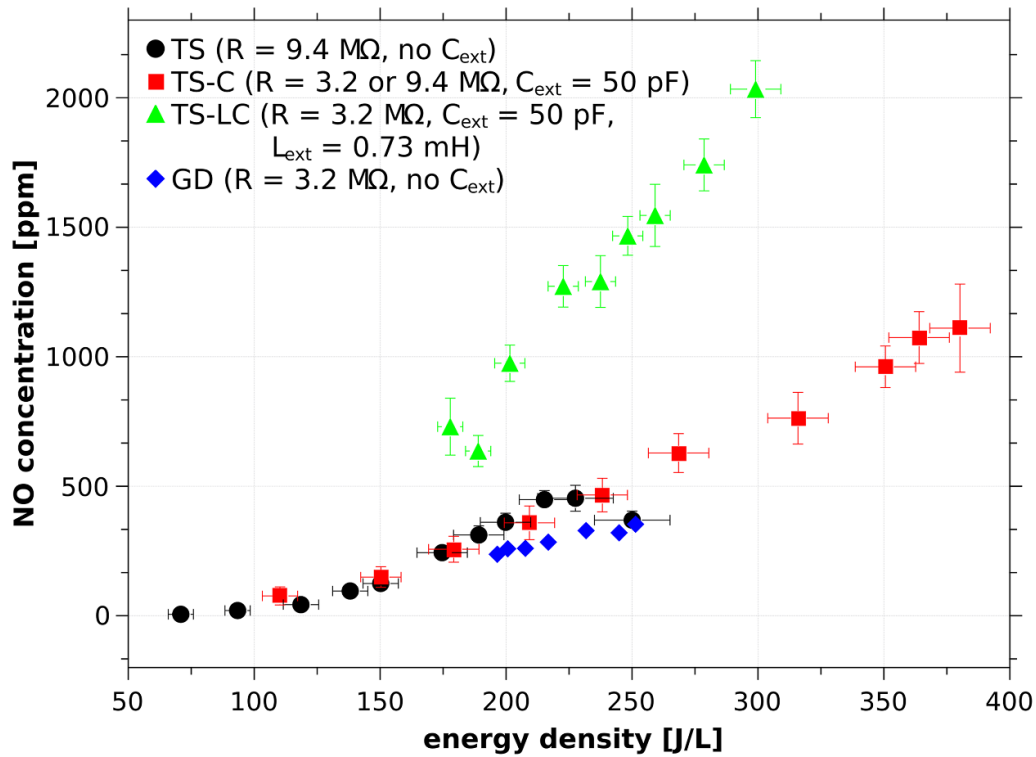


Figure 15. Influence of additional L_{ext} and C_{ext} on NO production in transient spark discharges, dry synthetic air, also compared with glow discharge (GD); Transient spark discharges generated with driving circuits without additional capacitor or inductor (TS), with an additional capacitor (TS-C) and with additional capacitor and inductor (TS-LC); values of ballast resistance (R), additional capacitance (C_{ext}) and additional inductance (L_{ext}) are indicated on the figure.

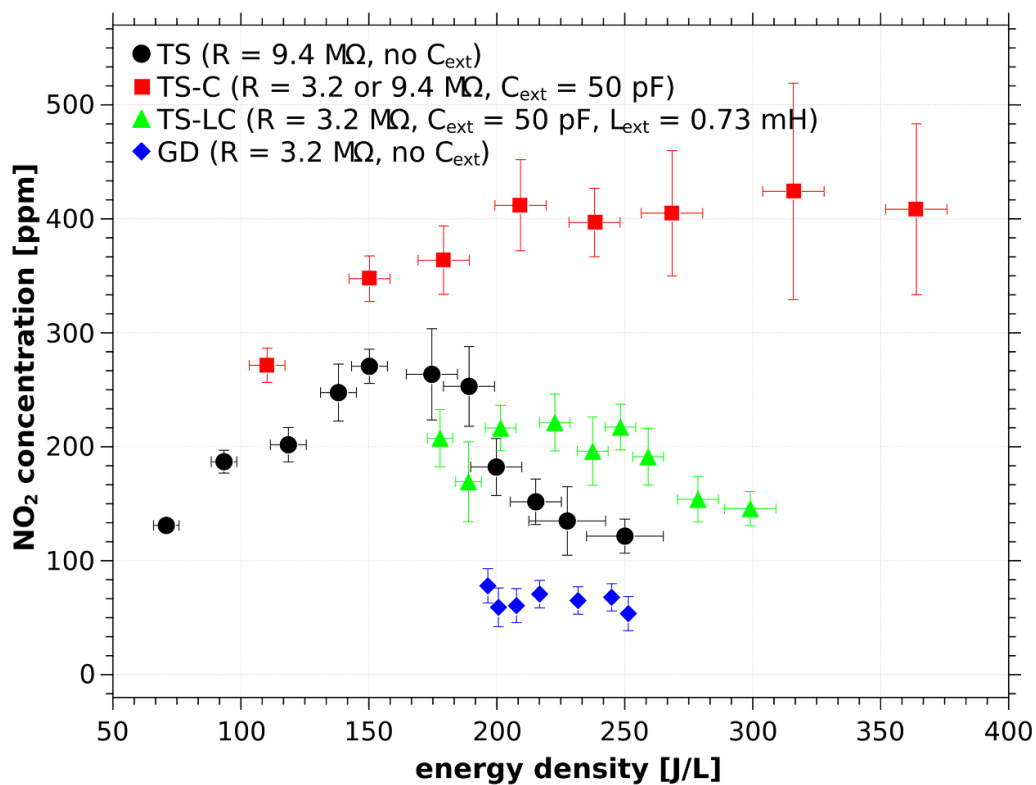


Figure 16. Influence of L_{ext} and C_{ext} on NO₂ production, dry synthetic air, transient spark discharges compared with glow discharge.

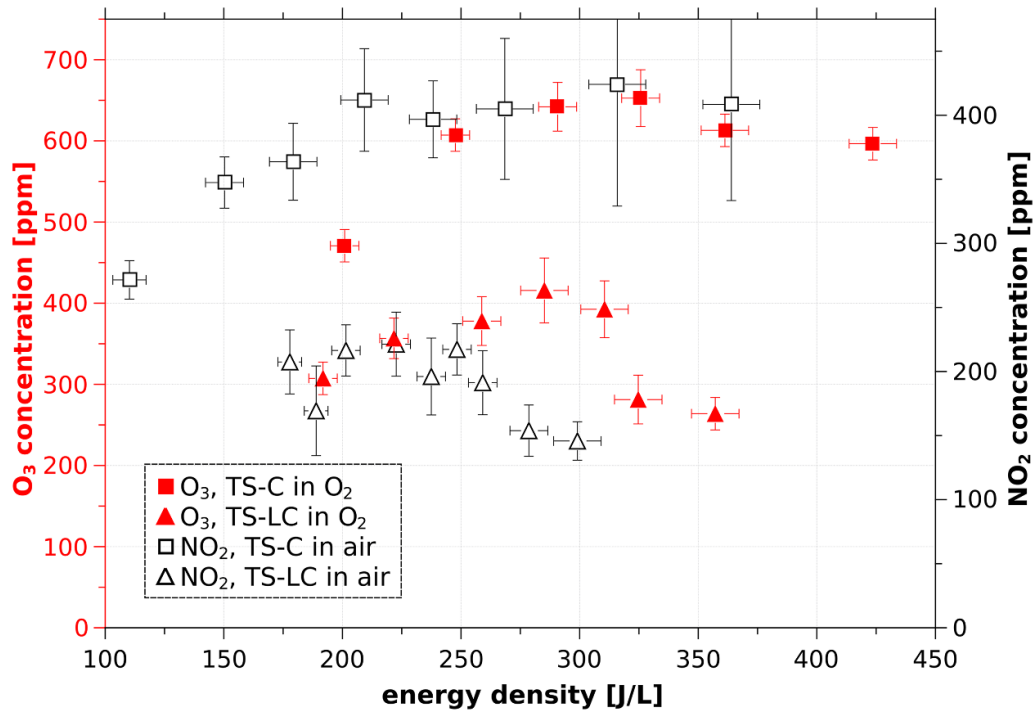


Figure 17. Comparison of O_3 concentration in O_2 gas with NO_2 concentration produced in dry synthetic air, TS-LC and TS-C, $C_{ext} = 50$ pF.

that the highest NO_2 concentrations were generated with just the additional capacitance, C_{ext} . The NO_2 concentration generated with L_{ext} and C_{ext} is similar to the concentration generated with the transient spark discharge with no additional circuit components. As noted above, we propose that the concentration of O_3 is critical to the formation of NO_2 . So again, experiments were performed in oxygen to investigate O_3 production with and without the additional inductor in the driving circuit.

Figure 17 shows concentrations of O_3 (left axis) generated by transient spark in oxygen with an additional capacitor (TS-C) and with an additional inductor and a capacitor (TS-LC) as a function of the input energy density. Again, with oxygen as the input gas the only significant gaseous product was O_3 . Figure 17 also shows the concentration of NO_2 (right axis) generated by both TS-C and TS-LC in dry air for comparison.

Similar to figure 7, the striking feature in figure 17 is the similarity of the trends of the O_3 and NO_2 concentrations. The O_3 concentration is higher in TS-C compared to TS-LC, which is consistent with higher concentration of NO_2 generated by TS-C in air. Moreover, the ratio of O_3 in TS-C to TS-LC is very similar to the ratio of NO_2 in TS-C to TS-LC. Again, the similarity of these ratios supports the hypothesis that NO_2 is mostly formed by reaction of O_3 with NO and that the higher concentration of NO_2 with the TS-C circuit compared to TS-LC is due to the higher concentration of O_3 . The reason for the higher concentration of O_3 with TS-C compared to TS-LC may be because the strong short pulses of TS-C give stronger gas mixing, faster cooling and no significant gas pre-heating in the gap by previous pulses. Another possibility is that the presence of additional inductor, L_{ext} , enhances NO generation shortly after the spark current pulse and when O_3 starts to be

produced, there are not so many O atoms remaining for O_3 generation, because they were used in the generation of NO .

4. Conclusions

Transient spark discharges are self-pulsing DC driven discharges, which generate highly reactive plasmas. The dominant products of transient spark discharges in air are NO and NO_2 . The energy efficiency of NO and NO_2 production depends on the driving circuit which generates the transient spark discharges. The NO concentration grows approximately linearly with increasing input energy density, but this increase is limited by the transition from transient spark discharge to GD, which occurs as the driving voltage increases. GD also generates NO and NO_2 , but the energy efficiency is lower. Transition to GD can be avoided by the addition of a capacitor of 50–500 pF. This inhibition of the GD mode allows smaller ballast resistors to be used, with lower energy losses. The addition of an external capacitor enables higher input energy densities to be used and enhanced concentrations of NO and NO_2 have been achieved; 1100 ppm and 400 ppm, respectively, at ~ 375 J l⁻¹.

Even higher concentration of NO and better energy efficiency were achieved by using an additional capacitor and an inductor of 0.73 mH in the driving circuit. The higher NO generation efficiency could be attributed to the prolongation of the active plasma phase. The addition of the inductor stretches the discharge pulse from less than one microsecond to at least 5–6 μ s after the primary current peak. During the prolongation there are several ‘re-breakdowns’ when the polarity of the potential driving the discharge reverses. NO concentrations

as high as 2000 ppm were achieved at input energy density around 300 J l^{-1} , though the NO_2 concentration was lower, 150 ppm. This driving circuit modification has potential to enable the scale up of this nitrogen fixation process because of the higher energy efficiency and higher yields achieved. Next step in the nitrogen fixation is the solvation of gaseous products into water. The solubility of NO_2 is better than the solubility of NO , it is therefore interesting finding to see higher efficiency of NO_2 formation in transient spark driving circuit with additional external capacitor. However, higher concentration of NO generated in the driving circuit with capacitor and inductor can be useful if humid air is treated to produce higher concentrations of HNO_2 having solubility even better than NO_2 .

Further research is therefore needed in humid air and with transient spark in contact with water to identify the most suitable configuration for the most efficient nitrogen fixation. In summary, the present results indicate that the influence of external inductors and capacitors on transient spark discharges properties is worth further research. For example, it would be also interesting to compare the energy efficiency of NO generation with different inductors.

Data availability statement

The data that support the findings of this study are openly available at the following URL/DOI: <https://doi.org/10.5281/zenodo.7630085> [53].

Acknowledgments

This work was supported by Slovak Research and Development Agency APVV-17-0382 and APVV-20-0566 and Slovak Grant Agency VEGA 1/0596/22 and 1/0822/21 and by COST Action CA19110 'PIAgri' (supported by European Cooperation in Science and Technology).

Ethics approval and consent to participate

Not applicable because there are no studies involving humans or animals.

Conflict of interest

The authors declare that there are no financial, personal or other conflicts of interest related to this work.

ORCID iDs

Mário Janda  <https://orcid.org/0000-0001-9051-4221>
 Karol Hensel  <https://orcid.org/0000-0001-6833-681X>
 Zdenko Machala  <https://orcid.org/0000-0003-1424-1350>
 Thomas A Field  <https://orcid.org/0000-0002-3394-1136>

References

- [1] Puač N, Gherardi M and Shiratani M 2018 Plasma agriculture: a rapidly emerging field *Plasma Process. Polym.* **15** 1700174
- [2] Kaushik N K et al 2019 *Biol. Chem.* **400** 39–62
- [3] Stancampiano A, Galligani T, Gherardi M, Machala Z, Maguire P, Colombo V, Pouvesle J-M and Robert E 2019 Plasma and aerosols: challenges, opportunities and perspectives *Appl. Sci.* **9** 3861
- [4] Čech J, Štáhel P, Ráhel J, Prokeš L, Rudolf P, Maršálková E and Maršálek B 2020 Mass production of plasma activated water: case studies of its biocidal effect on algae and cyanobacteria *Water* **12** 3167
- [5] Adamovich I et al 2022 The 2022 plasma roadmap: low temperature plasma science and technology *J. Phys. D: Appl. Phys.* **55** 373001
- [6] Jiang N, Guo L, Shang K, Lu N, Li J and Wu Y 2017 Discharge and optical characterizations of nanosecond pulse sliding dielectric barrier discharge plasma for volatile organic compound degradation *J. Phys. D: Appl. Phys.* **50** 155206
- [7] Homola T, Pongráč B, Zemánek M and Šimek M 2019 Efficiency of ozone production in coplanar dielectric barrier discharge *Plasma Chem. Plasma Process.* **39** 1227–42
- [8] Burlica R, Kirkpatrick M J and Locke B R 2006 Formation of reactive species in gliding arc discharges with liquid water *J. Electrostat.* **64** 35–43
- [9] Pavlovich M J, Ono T, Galleher C, Curtis B, Clark D S, Machala Z and Graves D B 2014 Air spark-like plasma source for antimicrobial NO_x generation *J. Phys. D: Appl. Phys.* **47** 505202
- [10] Pekárek S 2017 Experimental study of nitrogen oxides and ozone generation by corona-like dielectric barrier discharge with airflow in a magnetic field *Plasma Chem. Plasma Process.* **37** 1313–30
- [11] Liu Z, Xu D, Liu D, Cui Q, Cai H, Li Q, Chen H and Kong M G 2017 Production of simplex RNS and ROS by nanosecond pulse N_2/O_2 plasma jets with homogeneous shielding gas for inducing myeloma cell apoptosis *J. Phys. D: Appl. Phys.* **50** 195204
- [12] Reuter S, von Woedtke T and Weltmann K 2018 The kINPen—a review on physics and chemistry of the atmospheric pressure plasma jet and its applications *J. Phys. D: Appl. Phys.* **51** 233001
- [13] Nani L, Tampieri F, Ceriani E, Marotta E and Paradisi C 2018 ROS production and removal of the herbicide metolachlor by air non-thermal plasma produced by DBD, DC- and DC+ discharges implemented within the same reactor *J. Phys. D: Appl. Phys.* **51** 274002
- [14] Graves D B 2012 The emerging role of reactive oxygen and nitrogen species in redox biology and some implications for plasma applications to medicine and biology *J. Phys. D: Appl. Phys.* **45** 263001
- [15] Von Woedtke T, Reuter S, Masur K and Weltmann K-D 2013 Plasmas for medicine *Phys. Rep.* **530** 291–320
- [16] Moncada S, Palmer R M J and Higgs E A 1991 Nitric oxide: physiology, pathophysiology, and pharmacology *Pharmacol. Rev.* **43** 109–42 (available at: <https://pharmrev.aspetjournals.org/content/43/2/109>)
- [17] Cherkasov N, Ibhaddon A O and Fitzpatrick P 2015 A review of the existing and alternative methods for greener nitrogen fixation *Chem. Eng. Process.: Process Intensif.* **90** 24–33
- [18] Bruggeman P J et al 2016 *Plasma Sources Sci. Technol.* **25** 053002
- [19] Laurita R, Barbieri D, Gherardi M, Colombo V and Lukeš P 2015 Chemical analysis of reactive species and

- antimicrobial activity of water treated by nanosecond pulsed DBD air plasma *Clin. Plasma Med.* **3** 53–61
- [20] Girard F, Badets V, Blanc S, Gazeli K, Marlin L, Authier L, Svarnas P, Sojic N, Clément F and Arbault S 2016 Formation of reactive nitrogen species including peroxyxynitrite in physiological buffer exposed to cold atmospheric plasma *RSC Adv.* **6** 78457–67
- [21] Gorbanev Y, O'Connell D and Chechik V 2016 Non-thermal plasma in contact with water: the origin of species *J. Phys. D: Appl. Phys.* **22** 3496–505
- [22] Hsieh K C, Wandell R J, Bresch S and Locke B R 2017 Analysis of hydroxyl radical formation in a gas-liquid electrical discharge plasma reactor utilizing liquid and gaseous radical scavengers *Plasma Process. Polym.* **14** e1600171
- [23] Chauvin J, Judée F, Yousfi M, Vicendo P and Merbahi N 2017 Analysis of reactive oxygen and nitrogen species generated in three liquid media by low temperature helium plasma jet *Sci. Rep.* **7** 4562
- [24] Ito T, Uchida G, Nakajima A, Takenaka K and Setsuhara Y 2017 Control of reactive oxygen and nitrogen species production in liquid by nonthermal plasma jet with controlled surrounding gas *Jpn. J. Appl. Phys.* **56** 01AC06
- [25] Lu P, Boehm D, Bourke P and Cullen P J 2017 *Plasma Process. Polym.* **14** 1600207
- [26] Machala Z, Tarabová B, Sersenová D, Janda M and Hensel K 2018 *J. Phys. D: Appl. Phys.* **52** 034002
- [27] Alves Junior C, de Menezes F L G, Vitoriano J D and da Silva D L S 2019 Effect of plasma-activated water on soaking, germination, and vigor of erythrina velutina seeds *Plasma Med.* **9** 111–20
- [28] Rathore V, Tiwari B S and Nema S K 2021 Treatment of pea seeds with plasma activated water to enhance germination, plant growth, and plant composition *Plasma Chem. Plasma Process.* **42** 109–29
- [29] Sarangapani C, Scally L, Gulan M and Cullen P J 2020 Dissipation of pesticide residues on grapes and strawberries using plasma-activated water *Food Bioprocess Technol.* **13** 1728–41
- [30] Xu D H, Wang S, Li B, Qi M, Feng R, Li Q, Zhang H, Chen H and Kong M G 2020 Effects of plasma-activated water on skin wound healing in mice *Microorganisms* **8** 1091
- [31] Boehm D, Curtin J, Cullen P J and Bourke P 2018 Hydrogen peroxide and beyond-the potential of high-voltage plasma-activated liquids against cancerous cells *Anti-Cancer Agents Med. Chem.* **18** 815–23
- [32] Stratton G R, Bellona C L, Dai F, Holsen T M and Thagard S M 2015 *Chem. Eng. J.* **273** 543
- [33] Kruszelnicki J, Lietz A M and Kushner M J 2019 *J. Phys. D: Appl. Phys.* **52** 355207
- [34] Hassan M E, Janda M and Machala Z 2021 *Water* **13** 182
- [35] Burlica R, Grim R G, Shih K-Y, Balkwill D and Locke B R 2010 *Plasma Process. Polym.* **7** 640
- [36] Kanev I L, Mikheev A Y, Shlyapnikov Y M, Shlyapnikova E A, Morozova T Y and Morozov V N 2014 *Anal. Chem.* **86** 1511
- [37] Oinuma G, Nayak G, Du Y and Bruggeman P J 2020 *Plasma Sources Sci. Technol.* **29** 095002
- [38] Kovalova Z, Leroy M, Kirkpatrick M J, Odic E and Machala Z 2016 *Bioelectrochemistry* **112** 91
- [39] Janda M, Martišoviř V and Machala Z 2011 *Plasma Sources Sci. Technol.* **20** 035015
- [40] Janda M, Machala Z, Niklová A and Martišoviř V 2012 *Plasma Sources Sci. Technol.* **21** 045006
- [41] Janda M, Martišoviř V, Hensel K, Dvonč L and Machala Z 2014 *Plasma Sources Sci. Technol.* **23** 065016
- [42] Field T A, Harkin C, Asimakoulas L, Janda M, Hensel K and Machala Z 2023 submitted
- [43] Gordon I E, Boulet C and Tipping R H 2017 *J. Quant. Spectrosc. Radiat. Transfer* **203** 425–33
- [44] Kochanov R V et al 2019 *J. Quant. Spectrosc. Radiat. Transfer* **230** 172
- [45] Keller-Rudek H, Moortgat G K, Sander R and Sørensen R 2013 *Earth Syst. Sci. Data* **5** 365
- [46] Machala Z, Janda M, Hensel K, Jedlovský I, Leřtinská L, Foltin V, Martišoviř V and Morvová M 2007 *J. Mol. Spectrosc.* **243** 194
- [47] Capitelli M, Ferreira C M, Gordiets B F and Osipov A I 2000 *Plasma Kinetics in Atmospheric Gases* (Springer)
- [48] Wang W, Patil B, Heijkers, S, Hessel V and Bogaerts A 2017 *ChemSusChem* **10** 2145–57
- [49] Janda M, Hensel K and Machala Z 2019 *Proc. 22nd Symp. on Applications of Plasma Processes and 11th Eu-Japan Joint Symp. on Plasma Processing SAPP XXII (Strbske Pleso (Slovakia), 18–24 January)* pp 25–32
- [50] Atkinson R, Baulch D L, Cox R A, Crowley J N, Hampson R F, Hynes R G, Jenkin M E, Rossi M J and Troe J 2004 Evaluated kinetic and photochemical data for atmospheric chemistry: volume I-gas phase reactions of Ox, HOx, NOx and SOx species *Atmos. Chem. Phys.* **4** 1461–738
- [51] Hoder T, Bonaventura Z, Bourdon A and Simek M 2015 *J. Appl. Phys.* **117** 073302
- [52] Janda M, Hoder T, Sarani A, Brandenburg R and Machala Z 2017 *Plasma Sources Sci. Technol.* **26** 055010
- [53] Mario J, Karol H, Zdenko M and Field T A 2023 The influence of electric circuit parameters on NOx generation by transient spark discharge *Zenodo* (<https://doi.org/10.5281/zenodo.7630085>)